

## Substituent Effects

The Relationship between Structure and Properties in Zn<sup>II</sup> Complexes of Bulky *N,N'*-Diarylformamidinate *N*-OxidesMihaela Cibian,<sup>[a]</sup> Sophie Langis-Barsetti,<sup>[a]</sup> Janaina G. Ferreira,<sup>[a]</sup> and Garry S. Hanan<sup>\*[a]</sup>

**Abstract:** Homoleptic zinc(II) complexes (**3a–3d**) of the bulky *N,N'*-diarylformamidinate *N*-oxide ligands *N*-hydroxy-*N,N'*-bis(2,6-diisopropylphenyl)formamidine (**2a**), *N*-hydroxy-*N,N'*-bis(2,6-dimethylphenyl)formamidine (**2b**), *N*-hydroxy-*N,N'*-bis(2-isopropylphenyl)formamidine (**2c**) and *N*-hydroxy-*N,N'*-bis(2-biphenyl)formamidine (**2d**) were synthesized and characterized. Their solid-state structures are presented together with their solution properties, as examined by NMR and UV/Vis spectroscopy, and cyclic voltammetry. Theoretical calculations [DFT

and time-dependent DFT (TD-DFT)] were performed to assess and to rationalize the influence of ligand modification on the properties of the complexes: the highest occupied molecular orbital (HOMO), localized on the NCNO moiety, is less influenced by the substitution pattern, whereas the lowest unoccupied molecular orbital (LUMO), localized on the aryl ring with the O–N moiety, is directly affected; therefore, the optical band gap can be fine-tuned for potential applications.

## Introduction

The *N*-donor ligands 2,2'-bipyridine<sup>[1]</sup> and 2,2':6',2''-terpyridine<sup>[2]</sup> have been used widely in coordination chemistry as they form stable five-membered chelate rings upon metal-ion coordination. The metal complexes thus formed are typically cationic owing to the charge neutrality of the ligands, which makes them less useful in applications such as metal–organic frameworks.<sup>[3]</sup> The use of anionic ligands allows the formation of neutral metal complexes with favourable interactions between the metal ion and the ligand, which can be extended to oligo- or polymetallic assemblies. An appealing class of anionic ligands is the amidine *N*-oxide type (AMOX, also known as  $\alpha$ -aminonitrones and *N*-hydroxyamidines; Figure 1),<sup>[4]</sup> which has attracted relatively little attention from a coordination and supramolecular chemistry perspective. AMOXs are bidentate anionic ligands, good chelators for metal ions, and exhibit good electronic delocalization in the amidine backbone. Furthermore, their electronic and steric properties can be modulated and fine-tuned by variation of the substitution pattern on the amidine moiety (Figure 1).<sup>[4a,4d]</sup>

We are interested in the metal complexes of AMOX ligands because we can fine-tune the properties of the ligands to alter the corresponding properties of the complexes for applications in catalysis as well as luminescent and magnetic materials. For the AMOX-based metal complexes, the electron density at the metal ion can be influenced by changing the substituents on the N atoms, the central carbon atom of the amidine or both. By varying the donor ability of the N,O chelators (by using elec-

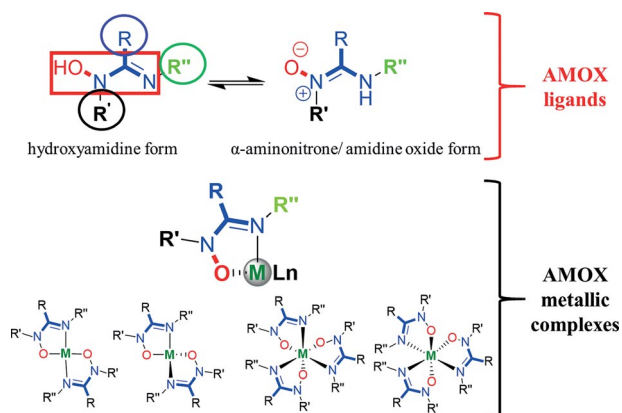


Figure 1. AMOX ligands and their metallic complexes.

tron-withdrawing or -donating groups, steric stimuli, or both), the metal–ligand interaction can be modulated to produce changes in the structure and geometry of the complexes and, hence, their properties. Our preliminary studies with Co<sup>II</sup>-(AMOX)<sub>2</sub> complexes showed that a rare square-planar geometry exists with a *d*<sup>7</sup> cobalt(II) centre in a bis-bidentate environment.<sup>[5]</sup> Isomerization from square-planar to tetrahedral geometry accompanied by a change in spin was also identified for these compounds.<sup>[6]</sup>

Herein, a combined experimental and theoretical analysis of a zinc(II) family of bis(AMOX)chelates is used to examine ligand influence in bis(AMOX)zinc(II) complexes. As electronic factors do not produce a preferred coordination geometry for zinc(II) ions, the tetrahedral geometry is favoured on steric grounds in a four-coordinate environment.<sup>[7]</sup> Furthermore, zinc(II) is highly abundant and nontoxic, which bodes well for its incorporation into photoluminescent compounds for optoelectronic applications,<sup>[8]</sup> as has already been demonstrated by the studies on

[a] Département de Chimie, Université de Montréal,  
2900 Édouard-Montpetit, Montréal, Québec H3T-1J4, Canada  
E-mail: garry.hanan@umontreal.ca  
<http://www.groupeenergieverte.ca>

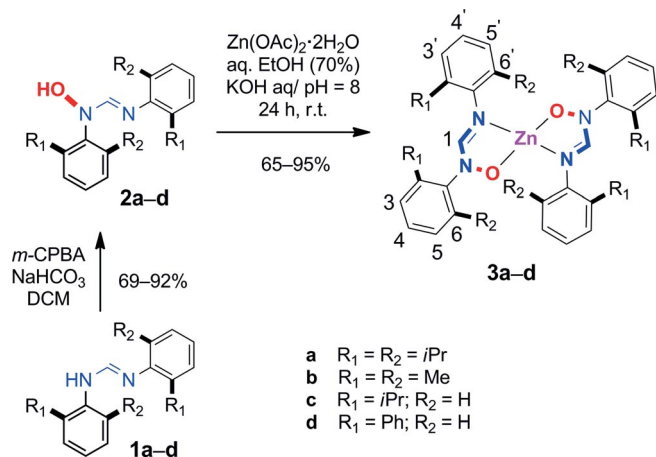
Supporting information for this article is available on the WWW under  
<http://dx.doi.org/10.1002/ejic.201501106>.

zinc(II) complexes of *N*-salicylidene-*N'*-aryylhydrazine ligands,<sup>[9]</sup> 8-hydroxyquinoline-type ligands,<sup>[10]</sup> benzothiazole and its derivatives,<sup>[11]</sup> and 2-oxazolylphenolate ligands.<sup>[12]</sup> Therefore, a theoretical approach, validated by comparison with experimental data, will allow us to develop the tools for the analysis of a broad family of AMOX-based compounds for the identification and synthesis of the right candidates for final use in device applications.

## Results and Discussion

### Synthesis

Formamidines **1a–1d** were synthesized from the corresponding anilines and triethyl orthoformate as described previously.<sup>[13]</sup> The syntheses of ligands **2a–2d** were realized in moderate-to-good yields (69–92 %) by the *N*-oxidation of their corresponding parent amidines with *meta*-chloroperoxybenzoic acid (*m*-CPBA) in dichloromethane (Scheme 1).<sup>[5,13e,14]</sup> Complexes **3a–3d** were prepared by reacting zinc(II) acetate with 2 equiv. of the corresponding ligand in aqueous ethanol at room temperature. The desired complexes precipitated readily in each case, and the products were isolated in good-to-excellent yields (65–95 %) as beige powders (Scheme 1). The solids are air-stable for months without decomposition. They dissolve readily in chlorinated solvents to give pale yellow solutions but are less soluble in polar solvents such as alcohols, *N,N*-dimethylformamide (DMF), and dimethyl sulfoxide (DMSO). The formation of the zinc bis(chelates) **3a–3d** was confirmed by mass spectrometry (MALDI) and elemental analysis. The complexes were also characterized in the solid state by X-ray crystallography (**3a**, **3b** and **3d**), and their properties in solution were investigated by <sup>1</sup>H NMR and UV/Vis spectroscopy as well as cyclic voltammetry.



Scheme 1. Synthesis of AMOX ligands **2a–2d** and their corresponding Zn(AMOX)<sub>2</sub> complexes **3a–3d**.

### <sup>1</sup>H NMR Spectroscopy

The <sup>1</sup>H NMR spectra for **3a–3d** are presented in Figure 2. Compounds **3a**, **3b**, and **3c** exhibit the characteristic doublet signals of the –CHCH<sub>3</sub> protons in the aliphatic region ( $\delta = 1.0$ –2.2 ppm).

The appearance of four doublet signals for the –CHCH<sub>3</sub> protons in **3a** upon complexation is in line with the diastereotopic nature of the protons. In addition, **3a** and **3c** show septet signals at chemical shifts between 3.2 to 4.0 ppm for the –CHCH<sub>3</sub> protons. The differences in the <sup>1</sup>H and <sup>13</sup>C NMR chemical shifts for the complexes with respect to those of the free ligands are indicative of the effect of metal-ion complexation. In all three cases, the signal corresponding to the C atom of the –N–CH=N– moiety appears downfield in the spectrum of the complex ( $\delta = 149$ –151 ppm) in comparison with the same signal for the free ligand ( $\delta = 142$ –147 ppm) as a result of the deshielding effect produced on coordination of the zinc(II) ion. The assignment of the <sup>1</sup>H NMR resonances was based on the integration ratios, 2D COSY, NOESY and heteronuclear multiple quantum correlation (HMQC) experiments as well as the proximity of the protons to the metal centre. The distinction between the *para*-4-H and *para*-4'-H protons (see Scheme 1 for the numbering) was proposed on consideration that the aryl ring attached to N–Zn is bound to a chelating N atom and is thus more influenced by the metal centre than the aryl ring bound to NO–Zn. As a consequence, *para*-4'-H is more deshielded than *para*-4-H.

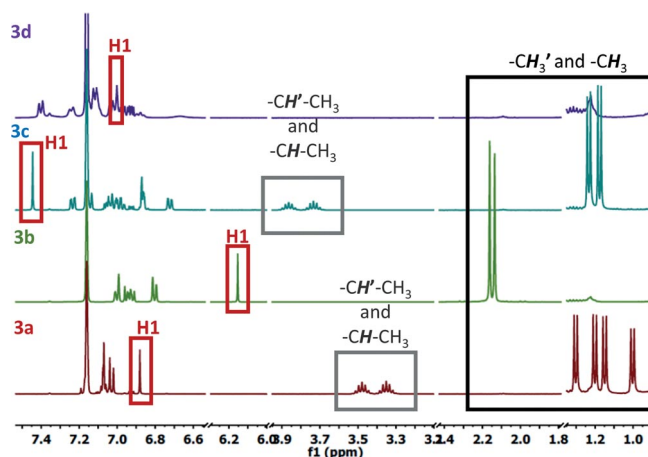


Figure 2. <sup>1</sup>H NMR spectra for **3a–3d** in C<sub>6</sub>D<sub>6</sub>.

In the spectrum of **3a** (Figure S1), the resonance of the –N–CH=N– proton H1 is shifted downfield with respect to those of the aliphatic substituents are shifted upfield with respect to those of **2a**. The same trend is maintained for **3b** and **2b** (Figure S2). However, for **3c** and **2c** (Figure S3), the signals of the –N–CH=N– protons H1 appear at similar chemical shifts, and the resonances of the aliphatic protons appear downfield. The deshielding influence of the coordination of the metal cation is combined with the shielding and deshielding effects resulting indirectly from the steric strain generated upon the formation of the complex, as the changes in the tilt angles between the plane of the –N=C–N–O– AMOX linkage and the planes of the *N*-aryl substituents dictate the degree of electron-density delocalization in the molecule (see X-ray Diffraction section). The difference in the substitution pattern of the aryl ring (2,6-disubstitution vs. 2-mono substitution) are important factors governing the interannular twist.

## X-ray Diffraction

Complexes **3a**, **3b** and **3d** were recrystallized from methanol (**3a** and **3b**) and dichloromethane (DCM, **3d**) to afford colourless X-ray-quality crystals. The molecular structures are shown in Figures 3, 4, 5 and S4–S10, and the crystal data, data collec-

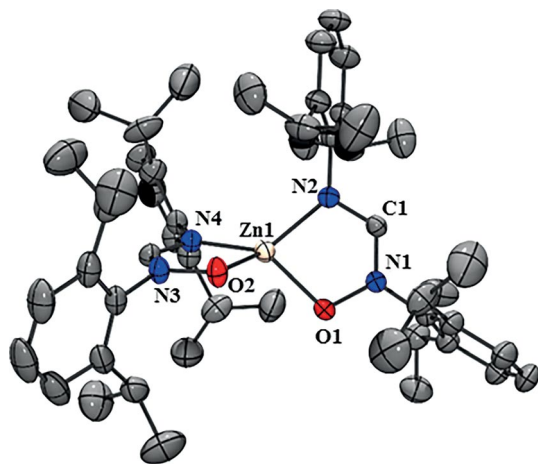


Figure 3. ORTEP view of **3a** with  $C_1$  symmetry. Ellipsoids are shown at 50 % probability level. Hydrogen atoms and cocrystallized solvent molecules are omitted for clarity.<sup>[15]</sup>

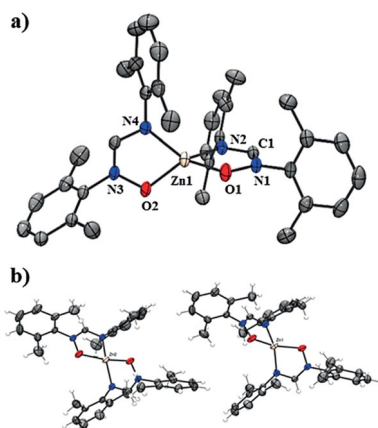


Figure 4. (a) ORTEP view of **3b**. Ellipsoids are shown at 50 % probability level. Hydrogen atoms are omitted for clarity. (b) The two molecules in the asymmetric unit.<sup>[15]</sup>

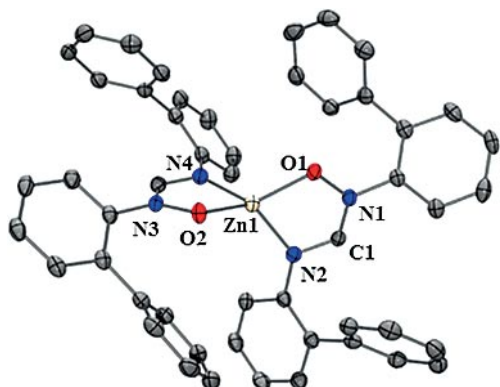


Figure 5. ORTEP view of **3d**. Ellipsoids are shown at 50 % probability level. Hydrogen atoms are omitted for clarity.<sup>[15]</sup>

tion and structure refinement details are summarized in Table 1. Selected bond lengths and angles for **3a**, **3b** and **3d** as well as other relevant zinc(II) bis(chelates) reported previously (**4–8**) are presented in Table 2. Compound **3b** crystallized with two independent molecules in the asymmetric unit (Figure 4). All three structures display monomeric zinc(II) ions in a pseudotetrahedral geometry with no coordinated solvent molecule or other strong interactions with atoms in their proximity. As mentioned previously, closed-shell  $d^{10}$  metal ions, especially those with bulky ligands, typically favour tetrahedral geometry on steric grounds in bis(bidentate) four-coordinate environments.<sup>[7,16]</sup> However, a Cambridge Structural Database (CSD)<sup>[17]</sup> search for tetrahedral zinc(II) complexes with bidentate N,O ligands in five-membered chelate rings yielded only eight crystal structures of this type,<sup>[18]</sup> in comparison with over 800 structures for their penta- or hexacoordinate analogues and over 200 structures for zinc(II) complexes with bidentate N,O ligands in six-membered chelate rings. Four of these eight structures correspond to zinc complexes of redox-active ligands of the *o*-aminophenol<sup>[19]</sup> and phenoxazin-1-one types.<sup>[20]</sup> In addition to the AMOXs, the other N,O ligands that form five-membered bis(chelates) of tetrahedral geometry with zinc(II) ions are  $[(Me_3Si)N(iPr_2PCO_2)]$ ,<sup>[21]</sup> triazene-1-oxide-type ligands<sup>[22]</sup> and sterically demanding 8-hydroxyquinoline derivatives.<sup>[23]</sup> The  $\tau_4$ <sup>[24]</sup> values are 0.73 for **3a**, 0.72 for **3b** and 0.77 for **3d**, and the periplanar angles ( $\gamma$ ; Table 2) between the two five-membered chelate rings are 70(1), 80(1) and 85(1)°, respectively. These values are indicative of a similar degree of distortion from a perfect tetrahedron in **3a** and **3b** (disubstitution pattern) and are also comparable with those for zinc(II) bis(chelates) of triazen-

Table 1. Solid-state structure and refinement data for **3a**, **3b** and **3d**.

	<b>3a</b>	<b>3b</b>	<b>3d</b>
Formula	$C_{50}H_{70}N_4O_4Zn \cdot 2(CH_3OH)_2$	$C_{34}H_{38}ZnN_4O_2$	$C_{50}H_{38}ZnN_4O_2$
$M_r$ [g/mol]	888.55	600.05	792.23
Temperature [K]	200	150	100
Wavelength [Å]	1.54178	1.54178	1.34139
Crystal System	triclinic	monoclinic	orthorhombic
<i>a</i> [Å]	11.6191(2)	8.7240(3)	19.3727(6)
<i>b</i> [Å]	11.9438(3)	30.8185(11)	7.8496(2)
<i>c</i> [Å]	21.8727(4)	24.0226(8)	24.8195(7)
$\alpha$ [°]	98.728(1)	90	90
$\beta$ [°]	94.086(1)	99.443(2)	90
$\gamma$ [°]	117.556(1)	90	90
Unit-cell volume [Å <sup>3</sup> ]	2625.0(1)	6371.2(4)	3774.3(1)
Space Group	$P\bar{1}$	$P2_1/n$	$Pca2_1$
<i>Z</i>	2	8	4
$d_{\text{calcd.}}$ [g/cm <sup>3</sup> ]	1.124	1.251	1.394
$\mu$ [mm <sup>-1</sup> ]	0.985	1.340	0.800
<i>F</i> (000)	960	2528	1648
Reflections collected	33981	82669	69171
Independent reflections	9932	12500	8671
GoF	1.086	0.943	1.040
<i>R</i> 1( <i>F</i> ) [ <i>I</i> > 2 $\sigma$ ( <i>I</i> )]	0.0491	0.0352	0.0404
<i>wR</i> ( <i>F</i> <sup>2</sup> ) [ <i>I</i> > 2 $\sigma$ ( <i>I</i> )]	0.1262	0.0912	0.0970
<i>R</i> 1( <i>F</i> ) (all data)	0.0542	0.0458	0.0515
<i>wR</i> ( <i>F</i> <sup>2</sup> ) (all data)	0.11298	0.0951	0.1035
Largest diff. peak and hole [e/Å <sup>3</sup> ]	0.414 and -0.549	0.269 and -0.435	1.17 and -0.22
Flack parameter	–	–	0.49(3)

1-oxides<sup>[22]</sup> and 8-hydroxyquinoline derivatives (**4** and **6**; Table 2).<sup>[23b]</sup> Furthermore, **3d** (monosubstitution pattern) is closer to a perfect tetrahedron, as are the corresponding zinc(II) complexes of *o*-aminophenol<sup>[19a]</sup> and  $\beta$ -ketoamine-type<sup>[25]</sup> ligands (**5** and **8**; Table 2). The Zn–O and Zn–N bond lengths are significantly different within the series of Zn(AMOX)<sub>2</sub> complexes reported herein, but they are still comparable within the series and with those found for similar structures.<sup>[22,23,25,26]</sup> In **3a**, the mean Zn–O bond length is 1.977(1) Å, whereas the same bond lengths in **3b** range between 1.987(1) and 1.992(1) Å (for the two molecules in the asymmetric unit). These values are close to those reported for tetrahedral zinc complexes of triazen-1-oxides<sup>[22]</sup> and 8-hydroxyquinoline derivatives (**4** and **6**; Table 2).<sup>[23b]</sup> The Zn–N bond lengths in **3a** and **3b** [1.981(1) Å and 1.963(1)–1.971(1) Å, respectively] are comparable with the corresponding values in **4**, as well as those in previously reported tetrahedral zinc complexes of  $\beta$ -ketoamine-type ligands (**8**; Table 2).<sup>[25]</sup> In **3d**, the mean Zn–O bond length [1.953(3) Å] is significantly shorter than those in **3a** and **3b** and is similar to the values reported for tetrahedral zinc(II) complexes of  $\beta$ -ketoamine-type ligands [1.953(1)–1.958(1) Å, **8**; Table 2].<sup>[25]</sup> The mean Zn–N bond length of 2.004(4) Å (in **3d**) is longer than those in **3a** and **3b** and is in the same range as those found in tetrahedral zinc complexes of *o*-aminophenol<sup>[19a]</sup> and 8-hydroxyquinoline derivatives (**5** and **6**, Table 2).<sup>[23b]</sup> The Zn–O and Zn–N bond lengths in **3a**, **3b** and **3d** are significantly longer than those reported for zinc complexes of Schiff base type ligands (**7**, Table 2);<sup>[27]</sup> planar geometry is forced by the macrocyclic nature of the ligand in the latter (the value of  $\tau_4$ <sup>[24]</sup> is 0.09). The different Zn–O and Zn–N bond lengths in **3a**, **3b** and **3d** are not reflected in the expansion or contraction of the O–N–C and N–C–N angles, which are equivalent in the three structures. Furthermore, the endocyclic O–Zn–N angles are also identical in all three compounds [84.1(1), 84.2(2) and 84.5(1)°, respectively]. The bite angle of the ligand and the strain of the five-membered chelate ring determine the contraction of this angle with respect to the ideal value. The mean O–N bond

lengths are identical in **3a**, **3b** and **3d**, and they are longer than those in triazene-1-oxide zinc complexes. All of the bond lengths in the AMOX moiety are identical for the three compounds; this supports the idea of the delocalization of electron density in the –N=C–N–O– AMOX linkage and allows the influence of the substituents on the Zn–O and Zn–N bonds and the geometry around the zinc(II) ion to be assessed. To accommodate the steric bulk generated by the 2,6-substituents of the aryl rings, the phenyl rings are pushed almost perpendicular to the plane of the chelate ring [the tilt angles in **3a** and **3b** are in the range 70(1)–89(1)°]; therefore, the electron density of the –N=C–N–O– AMOX linkage is less delocalized on the aromatic moieties of the ligand in **3a** and **3b**, whereas the 2-bi-phenyl-substituted analogue **3d** has more delocalization on the aromatic rings, as supported by values of the tilt angles of 42(1)° for Ar(NO) substituents and 45(1)° for Ar(N) substituents. The smaller tilt angles in **3a** [81(1)° for Ar(NO) and 70(1)° for Ar(N)] relative to those of **3b** [78(1)–89(1)° for Ar(NO) and 70(1)–76(1)° for Ar(N)] are explained by the greater repulsive interactions between the 2,6-diisopropyl substituents in **3a** than between the 2,6-dimethyl substituents in **3b**, for which the tilt angles are close to perpendicularity. In both **3a** and **3b**, the O atoms from the metal chelate rings are implicated in simple and bifurcated intra- and intermolecular hydrogen bonding. This type of interaction is a common feature for zinc(II) complexes with an O atom as at least one of the chelating atoms: 57 results were obtained in the CSD<sup>[17]</sup> for five-membered zinc(II) chelates of this type.<sup>[28]</sup> In **3a**, the O atoms interact with the ArN isopropyl protons (–CHCH<sub>3</sub>;  $d = 2.61$  Å,  $D = 3.35$  Å,  $\theta = 131^\circ$ , intramolecular) and with the –OH protons of the cocrystallized methanol molecules ( $d = 1.98$  Å,  $D = 2.80$  Å,  $\theta = 167^\circ$ ; Figure S8). In **3b**, the ArN methyl protons form intramolecular hydrogen bonds with the O atoms ( $d = 2.56$  Å,  $D = 3.44$  Å,  $\theta = 152^\circ$ ), and the ArNO methyl ( $d = 2.47$  Å,  $D = 3.38$  Å,  $\theta = 157^\circ$ ) and *m*-HC(sp<sup>2</sup>) protons ( $d = 2.62$  Å,  $D = 3.46$  Å,  $\theta = 150^\circ$ ) are implicated in weak intermolecular interactions of the same type (Figure S9). The participation of the O atoms in hydrogen-bonding

Table 2. Selected bond lengths [Å] and angles [°] for **3a**, **3b** and **3d** obtained from XRD and their optimized structures as well as examples of previously reported zinc bis(chelates) (**4**–**8**).

	$\tau_4$ <sup>[g]</sup>	Bond lengths / Å						Angle / ° Ar(NO) <sup>[j]</sup>	Tilt angles / °	
		Zn–O	Zn–N	C1–N1	C1–N2	O1–N1	O–Zn–N		ArN <sup>[j]</sup>	$\gamma$ <sup>[k]</sup>
<b>3a</b>	0.73	1.977(1) <sup>[h]</sup>	1.981(1) <sup>[h]</sup>	1.320(4) <sup>[h]</sup>	1.314(3) <sup>[h]</sup>	1.384(2) <sup>[h]</sup>	84.1(1) <sup>[h]</sup>	81(1) <sup>[h]</sup>	70(1) <sup>[h]</sup>	75(1)
<b>3b</b>	0.72	1.987(1)– 1.992(1) <sup>[i]</sup>	1.963(1)– 1.971(1) <sup>[i]</sup>	1.314(4) <sup>[h]</sup>	1.319(4) <sup>[h]</sup>	1.378(4) <sup>[h]</sup>	84.2(2) <sup>[h]</sup>	78(1)–89(1) <sup>[i]</sup>	70(1)– 76(1) <sup>[i]</sup>	80(1) <sup>[h]</sup>
<b>3d</b>	0.77	1.953(3) <sup>[h]</sup>	2.004(4) <sup>[h]</sup>	1.320(6) <sup>[h]</sup>	1.324(6)	1.378(5) <sup>[h]</sup>	84.5(1) <sup>[h]</sup>	42(1) <sup>[h]</sup>	45(1) <sup>[h]</sup>	85(1)
<b>4</b> <sup>[a]</sup>	0.74	1.967(4) <sup>[h]</sup>	1.968(4) <sup>[h]</sup>	–	–	1.330(4) <sup>[h]</sup>	80.3(1) <sup>[h]</sup>	–	7(1) <sup>[h]</sup>	86(1)
<b>5</b> <sup>[b]</sup>	0.77	1.924(1) <sup>[h]</sup>	2.052(1) <sup>[h]</sup>	–	–	–	85.7(1) <sup>[h]</sup>	–	–	84(1)
<b>6</b> <sup>[c]</sup>	0.68	1.997(3) <sup>[h]</sup>	2.037(4) <sup>[h]</sup>	–	–	–	83.5(1) <sup>[h]</sup>	–	–	85(1)
<b>7</b> <sup>[d]</sup>	0.09	1.851(1) <sup>[h]</sup>	1.871(1) <sup>[h]</sup>	–	–	–	91.2(1) <sup>[h]</sup>	–	–	37(1)
<b>8</b> <sup>[e]</sup>	0.79	1.953(1)– 1.958(1) <sup>[i]</sup>	1.966(1) <sup>[h]</sup>	–	–	–	96.4(1)–97.3(1) <sup>[i]</sup>	–	–	85(1)
<b>3a</b> -dft <sup>[f]</sup>	0.73	1.98 <sup>[h]</sup>	2.02 <sup>[h]</sup>	1.33 <sup>[h]</sup>	1.32 <sup>[h]</sup>	1.38 <sup>[h]</sup>	84 <sup>[h]</sup>	81–90 <sup>[i]</sup>	70 <sup>[h]</sup>	80
<b>3b</b> -dft <sup>[f]</sup>	0.78	1.99 <sup>[h]</sup>	2.01 <sup>[h]</sup>	1.33 <sup>[h]</sup>	1.32 <sup>[h]</sup>	1.38 <sup>[h]</sup>	84 <sup>[h]</sup>	83 <sup>[h]</sup>	73 <sup>[h]</sup>	90
<b>3d</b> -dft <sup>[f]</sup>	0.78	1.97 <sup>[h]</sup>	2.02 <sup>[h]</sup>	1.33 <sup>[h]</sup>	1.32 <sup>[h]</sup>	1.37 <sup>[h]</sup>	84 <sup>[h]</sup>	47 <sup>[h]</sup>	43 <sup>[h]</sup>	90

[a] **4**: Zn(RN<sub>3</sub>Ar)<sub>2</sub>.<sup>[22]</sup> [b] **5**: Zn(L)<sub>2</sub>, L = *o*-aminophenol-type ligand.<sup>[19a]</sup> [c] **6**: Zn(L)<sub>2</sub>, L = 8-hydroxyquinoline-type ligand.<sup>[23b]</sup> [d] **7**: Zn(L)<sub>2</sub>, L = [N<sub>2</sub>O<sub>2</sub>] Schiff base type ligand.<sup>[27]</sup> [e] **8**: Zn(L)<sub>2</sub>, L =  $\beta$ -ketoamine-type ligand.<sup>[25]</sup> [f] Optimized structures, theory level: B3LYP/6-31g(d, p), PCM: CH<sub>2</sub>Cl<sub>2</sub>. [g] As defined by Houser.<sup>[24]</sup> [h] Average value. [i] Range of values for the two molecules in the asymmetric unit. [j] Angle between the plane of the –N=C=N– moiety and the plane of the aromatic ring. [k] Periplanar angle between the two five-membered chelate rings.

interactions lowers their  $\pi$ -donation character and contributes to the observed pseudotetrahedral geometry around the zinc(II) ion in combination with the overall packing interactions and the steric bulk of the ligands. In **3d**, the O atoms are not implicated in hydrogen bonding. This, as well as the presence of attractive intramolecular interactions of the C(sp<sup>2</sup>)-H $\cdots$  $\pi$ C(sp<sup>2</sup>) type ( $d = 2.6$ – $3.5$  Å; Figure S10), could explain the shorter Zn–O bonds in this structure relative to those in **3a** and **3b**. Further examination of the packing interactions reveals nonclassical intermolecular hydrogen bonding of the  $\pi$ C(sp<sup>2</sup>) $\cdots$  $\pi$ C(sp<sup>2</sup>) type for **3b** and C(sp<sup>2</sup>)-H $\cdots$  $\pi$ C(sp<sup>2</sup>) type for **3b** and **3d**.

### UV/Vis Spectroscopic Properties

The spectroscopic data for the zinc(II) complexes **3a–3d** are summarized in Table 3. Their UV/Vis spectra in DCM are shown in Figure 6, together with those of the corresponding AMOX ligands **2a–2d**.

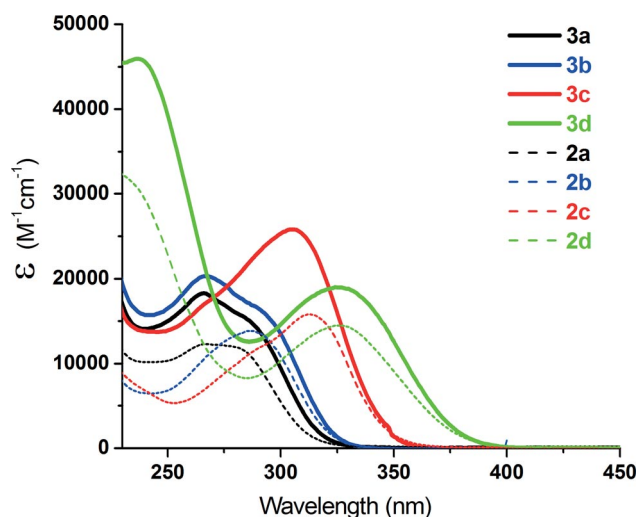


Figure 6. Electronic spectra of **3a–3d** and their corresponding ligands **2a–2d** in CH<sub>2</sub>Cl<sub>2</sub> at room temperature.  $\lambda_{\text{max}}$  [nm] ( $\epsilon \times 10^2$  [M<sup>-1</sup> cm<sup>-1</sup>]): **2a**: 280 (110); **2b**: 286 (130); **2c**: 293 sh (120), 313 (154); **2d**: 231 (321), 324 (145).

The electronic spectra of the compounds display the characteristic ligand-centred/intraligand (LC/IL)  $\pi$ – $\pi^*$  transitions in the UV region with high molar absorptivity coefficients, as expected for complexes with closed-shell d10 zinc(II) ions. Upon complex-

ation, slight redshifts of the lowest-energy absorption bands relative to those for the free ligands can be identified for **3a** and **3b**, whereas minor blueshifts are observed for **3c** and **3d**. For the same lowest-energy absorption band, a progressive redshift is observed across the **3a–3d** series. The intensity of this band varies as follows: the highest absorptivity coefficients are found for **3c** (25200 M<sup>-1</sup> cm<sup>-1</sup>) and **3d** (19000 M<sup>-1</sup> cm<sup>-1</sup>), followed by **3b** (15000 M<sup>-1</sup> cm<sup>-1</sup>) and **3a** (14800 M<sup>-1</sup> cm<sup>-1</sup>). The interpretation of the electronic spectra was greatly aided by time-dependent DFT (TD-DFT) calculations (vide infra).

### Electrochemistry

The redox properties of the Zn(AMOX)<sub>2</sub> complexes were also examined, and the data are reported in Table 3. The cyclic voltammograms (CVs) of **3a–3d** in dry DCM (Figure S11) display three irreversible ligand-based oxidation processes. The first two oxidations appear at similar potentials within the series [0.98–1.18 and 1.30 V–1.44 V vs. saturated calomel electrode (SCE), respectively], which indicates that substitution effects are minor. The third oxidation is the easiest in **3a** (1.63 V) followed by **3b** and **3c** (at similar potentials: 1.73 and 1.70 V, respectively) and then **3d** at 1.81 V; this series follows the increase in the electron-donating character of the ligands. It is important to mention that no reduction waves were observed for **3a–3d** in the electrochemical window of DCM; therefore, the lowest unoccupied molecular orbitals (LUMOs) are at high energies. The difficult reduction is in line with the anionic character of the ligand, enhanced by the effect of the electron-donating substituents, and was also reported for zinc(II) complexes of benzothiazole derivatives,<sup>[11]</sup> cobalt(II) complexes of electron-donating AMOX ligands<sup>[30]</sup> and cobalt complexes of triazene-1-oxides.<sup>[31]</sup> From the CVs of the compounds, the experimental energies of their highest occupied molecular orbitals (HOMOs) were determined (Figure 7, Table 3) from the onset potentials of the first oxidation waves ( $E_{\text{ox, onset}}$ ) by using the data versus SCE and the formula  $E_{\text{HOMO}}$  [eV] =  $-(4.4 + E_{\text{ox, onset}})$ .<sup>[9–12]</sup> As no reduction was observed for the compounds reported herein, the energies of the LUMOs were determined by using the equation  $E_{\text{LUMO}}$  [eV] =  $E_{\text{HOMO}} + E_g$ ;  $E_g$  is the optical band gap, obtained through the absorption-edge technique ( $E_g = 1240/\lambda_{\text{abs, onset}}$ ).<sup>[10c,32]</sup>

Table 3. Photophysical,<sup>[a]</sup> electrochemical<sup>[b]</sup> and theoretical<sup>[c]</sup> data for **3a–3d**.

	$\lambda_{\text{max}}$ [nm] ( $\epsilon \times 10^2$ [M <sup>-1</sup> cm <sup>-1</sup> ])	$E_{\text{pa}}$ (irr) [V] vs. SCE	Experimental data				Theoretical data			
			$E_{\text{ox, onset}}$ [V]	HOMO <sup>[d]</sup> [eV]	LUMO <sup>[e]</sup> [eV]	$E_g$ [f] [eV] ( $\lambda_{\text{abs, onset}}$ [nm])	HOMO <sup>[g]</sup> [eV]	LUMO <sup>[h]</sup> [eV]	$E_g$ (TD-DFT) <sup>[i]</sup> [eV]	
<b>3a</b>	270 (178), 287 (148) sh	1.17, 1.44, 1.63	1.04	-5.44	-1.54	3.90 (318)	-5.13	-1.17	3.96 (313)	
<b>3b</b>	267 (208), 296 (150) sh	1.18, 1.41, 1.73	1.07	-5.47	-1.64	3.83 (324)	-5.20	-1.33	3.87 (320)	
<b>3c</b>	270 (177), 304 (252)	0.98, 1.31, 1.70	0.86	-5.26	-1.98	3.60 (344)	–	–	–	
<b>3d</b>	237 (460), 325 (190)	1.03, 1.30, 1.81	0.88	-5.28	-2.10	3.28 (378)	-5.15	-1.66	3.49 (355)	

[a] The photophysical data were obtained in CH<sub>2</sub>Cl<sub>2</sub> at room temperature. [b] The electrochemical data were obtained under the following conditions: dry CH<sub>2</sub>Cl<sub>2</sub>, [nBu<sub>4</sub>N]PF<sub>6</sub> 0.1 M, compound concentration ca. 1 mM, glassy carbon electrode, scan rate 100 mV/s, room temperature, Ar atmosphere, ferrocene (Fc) as internal reference; Fc/Fc<sup>+</sup> versus SCE was considered to be 0.46 V in DCM.<sup>[29]</sup> [c] Theory level: B3LYP/6-31g(d, p), PCM: CH<sub>2</sub>Cl<sub>2</sub>. [d] The HOMO level was determined with the equation  $E_{\text{HOMO}}$  [eV] =  $-(4.4 + E_{\text{ox, onset}})$ . [e] No reduction process was observed; the LUMO level was determined with the equation  $E_{\text{LUMO}}$  [eV] =  $E_{\text{HOMO}} + E_g$ . [f]  $E_g$  was obtained through the absorption-edge technique:  $E_g = 1240/\lambda_{\text{abs, onset}}$ .<sup>[10c]</sup> [g] The HOMO level was obtained from DFT optimization, theory level: B3LYP/6-31g(d, p), PCM: CH<sub>2</sub>Cl<sub>2</sub>. [h] The LUMO level was obtained through  $E_{\text{LUMO}}$  [eV] =  $E_{\text{HOMO}}$  (DFT) +  $E_g$  (TD-DFT). [i]  $E_g$  (TD-DFT) is the TD-DFT-calculated first singlet, which corresponds to the HOMO–LUMO transition; theory level: B3LYP/6-31g(d, p), PCM: CH<sub>2</sub>Cl<sub>2</sub>.

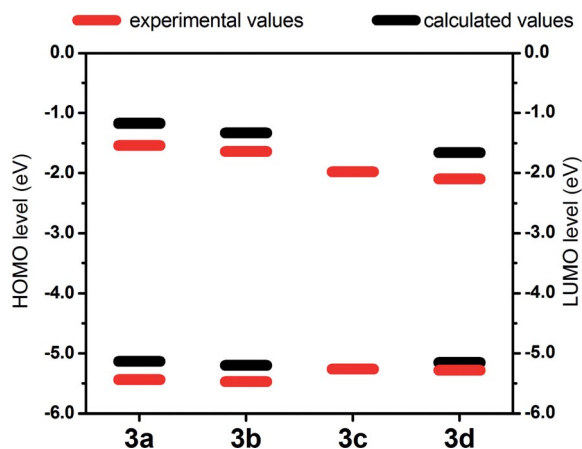


Figure 7. Experimental versus calculated band gaps for **3a–3d**.

### DFT and TD-DFT Calculations

DFT and TD-DFT calculations were performed for **3a**, **3b** and **3d** in dichloromethane [theory level B3LYP/6-31g(d,p), PCM: CH<sub>2</sub>Cl<sub>2</sub>]. This simple theoretical model has been applied to similar systems.<sup>[9–12,33]</sup> The optimized calculated structures are in good agreement with the XRD data (Table 2). The DFT and TD-DFT results support the experimental observations and are in very good agreement with the values obtained experimentally (Tables 2, 3 and 4, Figures 7, 8, 9 and S12–S15). In all three structures, the HOMO is localized on the –N=C–N–O– AMOX moiety (Figure 8, Table S1), without any contribution from the zinc(II) ion. As expected for a closed-shell d<sup>10</sup> metal ion, the zinc-based orbitals are very stable and are not involved in the redox or optical properties.

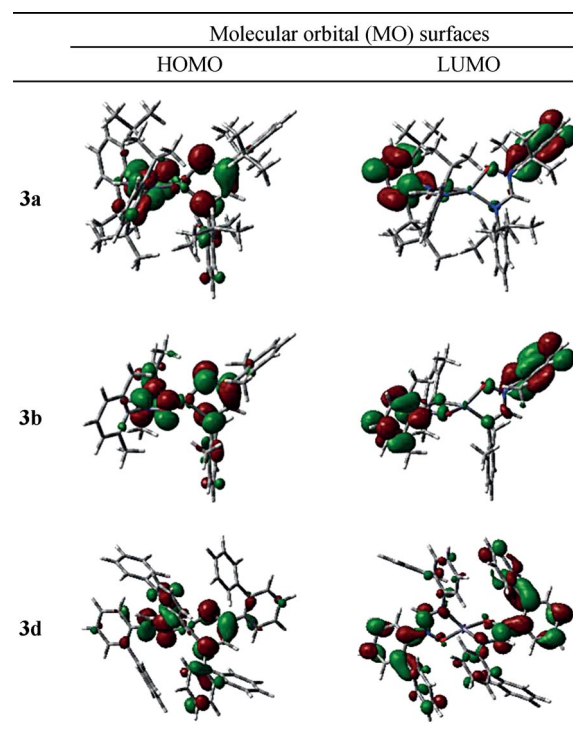


Figure 8. DFT-optimized structures of **3a–3d** with surfaces of the frontier molecular orbitals (MOs).

The localization of the HOMO on the AMOX moiety explains the substituent effect, in agreement with the electrochemical data. The LUMO is localized on Ar(NO) (the aryl ring with the N–O moiety attached, Figure 8, Table S1) and is, therefore, directly influenced by the substitution pattern and the degree of elec-

Table 4. TD-DFT-calculated lowest-energy singlet transitions for **3a–3d** with plots of the corresponding natural transition orbitals [NTOs; theory level: B3LYP/6-31g(d, p), PCM: CH<sub>2</sub>Cl<sub>2</sub>].

	$\lambda$ / nm (Oscillator strength)	Transition (% contribution)	NTO surfaces	
			'Hole'	'Particle'
<b>3a</b>	313 (0.0033)	HOMO→LUMO (76) H-1→L+1 (19)		
<b>3b</b>	320 (0.0089)	HOMO→LUMO (75) H-1→L+1 (23)		
<b>3d</b>	355 (0.0902)	HOMO→LUMO (67) H-1→L+1 (30)		

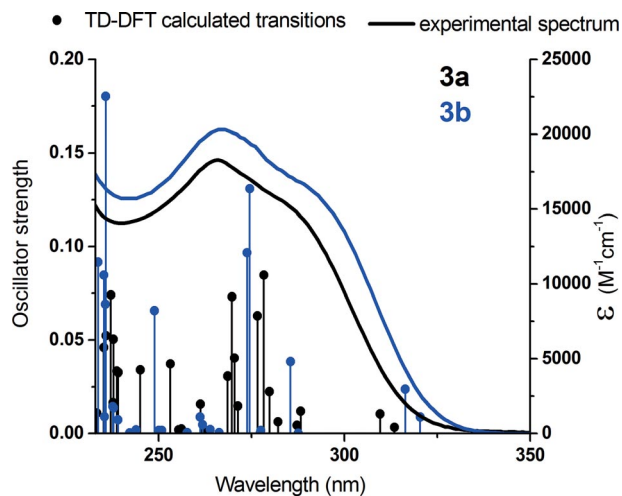


Figure 9. Electronic spectra of **3a** (in black) and **3b** (in blue) in  $\text{CH}_2\text{Cl}_2$ : experimental spectra and TD-DFT-calculated transitions (vertical lines), theory level: B3LYP/6,31-g(d,p), PCM:  $\text{CH}_2\text{Cl}_2$ .

tron-density delocalization on the respective aryl ring. Enhanced delocalization lowers the LUMO level and, therefore, decreases the band gap. Thus, the DFT and TD-DFT results confirm and explain the redshift of the lowest-energy electronic transition observed in the UV/Vis spectra of **3a–3d**, in line with the higher degree of delocalization in **3d** and **3c** versus **3a** and **3b** (Tables 3, 4 and S2–S4; Figures 7, 8, 9 and S12–S15). The trend is consistent with the values of the tilt angles between the N=C–N plane and the aryl rings attached to the N(ArN) and N–O [Ar(NO)] moieties and the bulkiness of the substituents (Table 2).

The order of increasing intensity of the electronic transitions (**3a** < **3b** < **3d**) is also reproduced by the TD-DFT calculations: the oscillator strength calculated for **3a** is the lowest, followed by those of **3b** and **3d** (Tables 3, 4 and S2–S5; Figures 9 and S12–S15).

In addition, the change in ligand conformation upon metal-ion complexation increases the energy of the LUMO relative to those for the free ligands, because the electron-density delocalization is decreased owing to the “decoupling” of the Ar(NO) ring from the  $\pi$  system of the AMOX, as indicated by the tilt angles of 78–89° for **3a** and **3b** and 42° for **3d**. The complexation influence on the energy of the HOMO with respect to the free ligands is the result of combined phenomena of opposite effects: the presence of increased electron density with reduced delocalization leads to destabilization, whereas stabilization is generated as the zinc(II) cation withdraws electron density from the –N=C–N–O– AMOX bridge. Further analysis of the TD-DFT calculations (Tables 4 and S2–S4, Figures 9 and S12–S15) indicates a strong correlation of the experimental data with the corresponding calculated transitions. The assignment of the electronic transitions for **3a**, **3b** and **3d** confirms the nature of the lowest-energy transition (HOMO–LUMO, Table 4). The subsequent electronic transitions at higher energies are also well modelled, and their detailed descriptions are presented in Tables S2–S4.

## Conclusions

The AMOX complexes described herein allowed the effect of N-substitution on the metal–ligand interaction as well as structural, spectroscopic and electrochemical properties to be examined. Bulky substituents at the 2,6-positions increase the electronic density in the amidine-oxide backbone by disrupting electron delocalization on the N atoms of the molecule (electronic effect induced by steric modification). This substitution pattern also prevents additional coordination to the metal ion and contributes to an enhanced solubility of the compounds. The theoretical calculations (DFT and TD-DFT) undertaken allowed the assessment and the rationalization of the influence of ligand modification on the properties of the complexes. The AMOX ligand family shows great promise for the preparation of a wide variety of transition-metal complexes with predictable and tuneable properties.

## Experimental Section

**Materials and Instrumentation:** The metal salts, anilines and triethyl orthoformate were purchased from Aldrich, and *m*-CPBA (77 %) was purchased from Acros; all were used without further purification. ACS-grade solvents were purchased from VRW and Fisher and were removed under reduced pressure with a rotary evaporator, unless otherwise stated. The NMR spectra of samples in  $[\text{D}_6]\text{DMSO}$ ,  $\text{C}_6\text{D}_6$  and  $\text{CDCl}_3$  at 25 °C were recorded with Bruker AV-400, AV-500 and DRX-400 spectrometers. Chemical shifts ( $\delta$ ) are reported in ppm relative to tetramethylsilane (TMS) and were referenced to the residual solvent signals ( $\delta = 2.50$  ppm for  $[\text{D}_6]\text{DMSO}$ , 7.16 ppm for  $\text{C}_6\text{D}_6$ , and 7.26 ppm for  $\text{CDCl}_3$ ). The absorption spectra of samples in dichloromethane (previously distilled) at room temp. were recorded between 230 and 1400 nm with a Cary 500i UV/Vis/NIR spectrophotometer. Solution samples were prepared in the concentration range  $10^{-5}$  to  $10^{-3}$  M. The electrochemical measurements were performed in argon-purged dry DCM at room temperature with a BAS CV50W multipurpose potentiostat. The working electrode was a glassy carbon electrode. The counter electrode was a Pt wire, and the pseudoreference electrode was a silver wire. The reference was an internal 1 mm ferrocene/ferrocenium sample at 460 and 450 mV vs. SCE in DCM.<sup>[29]</sup> The compound concentration was ca. 1 mM. Tetrabutylammonium hexafluorophosphate (TBAP) was used as the supporting electrolyte at a concentration of 0.10 M. Cyclic voltammograms were obtained at scan rates of 50, 100, 200 and 500 mV/s. For irreversible oxidation processes, the anodic peak was used as *E*. The experimental uncertainties were as follows: absorption maxima,  $\pm 2$  nm; molar absorption coefficient, 10 %; redox potentials,  $\pm 10$  mV. The microanalyses and the mass spectrometry analyses were performed at the Elemental Analysis Service and the Regional Mass Spectrometry Centre at Université de Montréal.

**X-ray Structure Determination:** The crystal structure determination and refinement data for **3a**, **3b** and **3d** are given in Tables 1 and 2 and Figures 3–5. Full details are provided in the Supporting Information.

CCDC-963739 (for **3b**), -963740 (for **3a**) and -1426815 (for **3d**) contain the supplementary crystallographic data for this paper. These data can be obtained free of charge via [www.ccdc.cam.ac.uk/data\\_request/cif](http://www.ccdc.cam.ac.uk/data_request/cif).

**Computational Details:** Gaussian09, Revision D.01<sup>[34]</sup> was used for all theoretical calculations discussed herein with the B3LYP<sup>[35]</sup> DFT

method, 6,31-g(d,p)<sup>[36]</sup> basis set and the polarizable continuum model (PCM)<sup>[37]</sup> for solvation (CH<sub>2</sub>Cl<sub>2</sub>). The initial atom coordinates for geometry optimization were taken from the XRD data (cif files) of the corresponding structures. No symmetry constraints were used for the geometry optimization. Details of the optimized structures are given in Tables S5–S7. No imaginary frequencies were obtained when frequency calculations were performed on the optimized geometries. TD-DFT<sup>[38]</sup> calculations [for the first 30 (**3a**, **3b**) and 50 (**3d**) singlet states] were performed for the optimized geometries of the ground states. GaussView 3.0.9,<sup>[39]</sup> Gausssum<sup>[40]</sup> and Chemission V4.36<sup>[41]</sup> were used for data analysis, visualization and surface plots.

**Compounds 1a–1d and 2a–2d:** The syntheses of the AMOX ligands **2a–2d**<sup>[5,13e,14]</sup> and their parent amidines **1a–1d**<sup>[13]</sup> were reported previously.

**General Procedure for the Synthesis of Complexes:**<sup>[4c,5]</sup> A solution of the ligand (2 equiv.) in aqueous ethanol 90 % was added to a solution of metal salt (1 equiv.) in water, which was previously brought to pH 8 with an aqueous solution of KOH or NaOH. The formation of a precipitate was observed almost instantly. The reaction mixture was stirred at room temperature, water was added (the reaction times are specified below for each compound), and the mixture was kept at 4 °C for 1–2 h. The resultant solid was collected by filtration, washed with hot water and aqueous ethanol 50 %, dissolved in DCM and dried with MgSO<sub>4</sub>. A second filtration and evaporation of the solvent yielded the desired products as solids. If necessary, further purification by recrystallization was performed.

**Complex 3a:** The following reagents were combined according to the general procedure: *N*-hydroxy-*N,N'*-bis(2,6-diisopropylphenyl)-formamidine (0.26 g, 0.69 mmol, 2 equiv.) and Zn<sup>II</sup> acetate·2H<sub>2</sub>O (0.08 g, 0.35 mmol, 1 equiv.). Reaction time: 24 h. The resulting colourless solid was recrystallized from hot methanol to afford colourless crystals, yield 0.27 g, 95 %. X-ray-quality crystals were obtained by the same recrystallization procedure. <sup>1</sup>H NMR (C<sub>6</sub>D<sub>6</sub>, 400 MHz): δ = 7.19 [m, 1 H, *p*-C<sub>6</sub>H<sub>3</sub>(N) (4'-H)], 7.11–7.02 [m, 5 H, *m*-C<sub>6</sub>H<sub>3</sub>(NO) (3-H and 5-H), *p*-C<sub>6</sub>H<sub>3</sub>(NO) (4-H), *m*-C<sub>6</sub>H<sub>3</sub>(N) (3'-H and 5'-H)], 6.89 [s, 1 H, -NCH=N- (1-H)], 3.48 (sept, *J* = 7 Hz, 2 H, -CHCH<sub>3</sub> or -CH'CH<sub>3</sub>), 3.35 (sept, *J* = 7 Hz, 2 H, -CHCH<sub>3</sub> or -CH'CH<sub>3</sub>), 1.30 (d, *J* = 7 Hz, 6 H, -CHCH<sub>3</sub> or -CHCH<sub>3</sub>'), 1.20 (d, *J* = 7 Hz, 6 H, -CHCH<sub>3</sub> or -CHCH<sub>3</sub>'), 1.15 (d, *J* = 7 Hz, 6 H, -CHCH<sub>3</sub> or -CHCH<sub>3</sub>'), 1.00 (d, *J* = 7 Hz, 6 H, -CHCH<sub>3</sub> or -CHCH<sub>3</sub>') ppm. <sup>13</sup>C NMR (C<sub>6</sub>D<sub>6</sub>, 101 MHz): δ = 150.0 (1 C, -NCH=N-), 147.7 (2 C, *o*-C<sub>6</sub>H<sub>3</sub>), 143.4 (2 C, *o*-C<sub>6</sub>H<sub>3</sub>), 143.2 (1 C, -C<sub>6</sub>H<sub>3</sub>), 138.5 (1 C, -C<sub>6</sub>H<sub>3</sub>), 129.8 (1 C, *p*-C<sub>6</sub>H<sub>3</sub>), 125.3 (1 C, *p*-C<sub>6</sub>H<sub>3</sub>), 123.8 (2 C, *m*-C<sub>6</sub>H<sub>3</sub>), 123.3 (2 C, *m*-C<sub>6</sub>H<sub>3</sub>), 28.86 (2 C, -CHCH<sub>3</sub>), 28.19 (2 C, -CHCH<sub>3</sub>), 24.96 (2 C, -CHCH<sub>3</sub>), 24.65 (2 C, -CHCH<sub>3</sub>), 24.59 (2 C, -CHCH<sub>3</sub>), 23.12 (2 C, -CHCH<sub>3</sub>) ppm. C<sub>50</sub>H<sub>70</sub>N<sub>4</sub>O<sub>2</sub>Zn (824.51): calcd. C 72.84, H 8.56, N 6.80; found C 72.19, H 8.63, N 6.76. MS (MALDI): *m/z* = 823.49 [M + H]<sup>+</sup>. IR [attenuated total reflectance (ATR), solid sample]:  $\tilde{\nu}$  = 3065, 3009, 2961, 2927, 2867, 1606, 1581, 1459, 1439, 1382, 1361, 1324, 1304, 1254, 1215, 1191, 1164, 1147, 1100, 1059, 1044, 998, 928, 816, 803, 761, 729, 682, 618, 582, 532, 491, 476, 456, 432 cm<sup>-1</sup>.

**Complex 3b:** The following reagents were combined according to the general procedure: *N*-hydroxy-*N,N'*-bis(2,6-diisopropylphenyl)-formamidine (0.50 g, 1.9 mmol, 2 equiv.) and Zn<sup>II</sup> acetate·2H<sub>2</sub>O (0.20 g, 0.9 mmol, 1 equiv.). Reaction time: 24 h. The resulting colourless solid was recrystallized from DCM/hexane to afford a pale beige powder, yield 0.37 g, 65 %. X-ray-quality crystals were obtained from methanol/water by slow diffusion at 4 °C and from [D<sub>6</sub>]DMSO by slow evaporation. <sup>1</sup>H NMR (C<sub>6</sub>D<sub>6</sub>, 400 MHz): δ = 7.00 [d, *J* = 7 Hz, 2 H, *m*-C<sub>6</sub>H<sub>3</sub>(N) (3'-H and 5'-H)], 6.96–6.91 [m, 2 H, *p*-C<sub>6</sub>H<sub>3</sub>(N) and *p*-C<sub>6</sub>H<sub>3</sub>(NO) (4'-H and 4-H)], 6.81 [d, *J* = 7 Hz, 2 H, *m*-

C<sub>6</sub>H<sub>3</sub>(N) (3-H and 5-H)], 6.16 [s, 1 H, -NCH=N- (1-H)], 2.16 (s, 6 H, CH<sub>3</sub>), 2.14 (s, 6 H, CH<sub>3</sub>') ppm. <sup>1</sup>H NMR ([D<sub>6</sub>]DMSO, 400 MHz): δ = ppm: 7.84 [s, 1 H, -NCH=N- (1-H)], 7.19 [t, *J* = 8 Hz, 1 H, *p*-C<sub>6</sub>H<sub>3</sub>(N) (4'-H)], 7.11 [d, *J* = 8 Hz, 2 H, *m*-C<sub>6</sub>H<sub>3</sub>(N) (3'-H and 5'-H)], 6.98 [d, *J* = 8 Hz, 2 H, *m*-C<sub>6</sub>H<sub>3</sub>(NO) (3-H and 5-H)], 6.88 [t, *J* = 8 Hz, 1 H, *p*-C<sub>6</sub>H<sub>3</sub>(NO) (4-H)], 2.17 (s, 6 H, CH<sub>3</sub>'), 1.97 (s, 6 H, CH<sub>3</sub>) ppm. <sup>13</sup>C NMR ([D<sub>6</sub>]DMSO, 75 MHz): δ = 149.6 (1 C, -NCH=N-), 145.1 (1 C, -C<sub>6</sub>H<sub>3</sub>), 140.3 (1 C, -C<sub>6</sub>H<sub>3</sub>), 135.9 (2 C, *o*-C<sub>6</sub>H<sub>3</sub>), 132.0 (2 C, *o*-C<sub>6</sub>H<sub>3</sub>), 128.5 (1 C, *p*-C<sub>6</sub>H<sub>3</sub>), 127.9 (2 C, *m*-C<sub>6</sub>H<sub>3</sub>), 127.7 (2 C, *m*-C<sub>6</sub>H<sub>3</sub>), 123.7 (1 C, *p*-C<sub>6</sub>H<sub>3</sub>), 18.11 (2 C, CH<sub>3</sub>), 16.90 (2 C, CH<sub>3</sub>) ppm. C<sub>34</sub>H<sub>38</sub>N<sub>4</sub>O<sub>2</sub>Zn (600.08): calcd. C 68.05, H 6.38, N 9.34; found C 67.65, H 6.90, N 9.30. MS (MALDI): *m/z* = 599.24 [M + H]<sup>+</sup>. IR (ATR, solid sample):  $\tilde{\nu}$  = 2917, 1611, 1582, 1470, 1373, 1306, 1203, 1089, 994, 929, 765, 687, 591, 531 cm<sup>-1</sup>.

**Complex 3c:** The following reagents were combined according to the general procedure: *N*-hydroxy-*N,N'*-bis(2-isopropylphenyl) formamidine (0.2 g, 0.7 mmol, 2 equiv.) and Zn<sup>II</sup> acetate·2H<sub>2</sub>O (0.07 g, 0.33 mmol, 1 equiv.). Reaction time: 24 h. A colourless solid was obtained, yield 0.07 g, 78 %. <sup>1</sup>H NMR (C<sub>6</sub>D<sub>6</sub>, 300 MHz, TMS): δ = 7.44 [s, 1 H, -NCH=N- (1-H)], 7.23 [d, *J* = 7 Hz, 1 H, *o*-C<sub>6</sub>H<sub>3</sub>(N) (6'-H)], 7.13 [d, 1 H, *o*-C<sub>6</sub>H<sub>3</sub>(NO) (6-H)], 7.10–6.94 [m, 3 H, *m*-C<sub>6</sub>H<sub>3</sub>(NO) (5-H), *m*-C<sub>6</sub>H<sub>3</sub>(N) (5'-H), *p*-C<sub>6</sub>H<sub>3</sub>(N) (4'-H)], 6.89–6.83 [m, 2 H, *p*-C<sub>6</sub>H<sub>3</sub>(NO) (4-H), *m*-C<sub>6</sub>H<sub>3</sub>(NO) (3-H)], 6.72 [d, *J* = 7 Hz, 1 H, *m*-C<sub>6</sub>H<sub>3</sub>(N) (3'-H)], 3.86 (sept, *J* = 7 Hz, 1 H, -CHCH<sub>3</sub> or -CH'CH<sub>3</sub>), 3.72 (sept, *J* = 7.0 Hz, 1 H, -CHCH<sub>3</sub> or -CH'CH<sub>3</sub>), 1.23 (d, *J* = 7 Hz, 6 H, -CHCH<sub>3</sub> or -CHCH<sub>3</sub>'), 1.18 (d, *J* = 7 Hz, 6 H, -CHCH<sub>3</sub> or -CHCH<sub>3</sub>') ppm. <sup>13</sup>C NMR (C<sub>6</sub>D<sub>6</sub>, 101 MHz, TMS): δ = 149.00 (1 C, -NCH=N-), 146.32 (1 C, C<sub>6</sub>H<sub>4</sub>), 145.76 (1 C, C<sub>6</sub>H<sub>4</sub>), 141.92 (1 C, C<sub>6</sub>H<sub>4</sub>), 141.12 (1 C, C<sub>6</sub>H<sub>4</sub>), 128.95 (1 C, *o*-C<sub>6</sub>H<sub>4</sub> or *p*-C<sub>6</sub>H<sub>4</sub>), 126.97 (1 C, *o*-C<sub>6</sub>H<sub>4</sub>), 126.67 (1 C, *o*-C<sub>6</sub>H<sub>4</sub> or *p*-C<sub>6</sub>H<sub>4</sub>), 126.42 (1 C, *o*-C<sub>6</sub>H<sub>4</sub>), 126.30 (1 C, *o*-C<sub>6</sub>H<sub>4</sub> or *p*-C<sub>6</sub>H<sub>4</sub>), 124.56 (1 C, *o*-C<sub>6</sub>H<sub>4</sub> or *p*-C<sub>6</sub>H<sub>4</sub>), 123.26 (1 C, *m*-C<sub>6</sub>H<sub>3</sub>), 28.55 (1 C, -CHCH<sub>3</sub>), 27.69 (1 C, -CHCH<sub>3</sub>), 24.07 (2 C, -CHCH<sub>3</sub>), 24.00 (2 C, -CHCH<sub>3</sub>) ppm. C<sub>38</sub>H<sub>46</sub>N<sub>4</sub>O<sub>2</sub>Zn (656.19): calcd. C 69.56, H 7.07, N 8.54; found C 69.52, H 6.92, N 8.53. IR (ATR, solid sample):  $\tilde{\nu}$  = 3053, 3028, 2961, 2926, 2867, 1609, 1587, 1571, 1487, 1446, 1386, 1360, 1341, 1326, 1282, 1240, 1195, 1163, 1085, 1036, 1002, 942, 905, 760, 751, 725, 665, 621, 603, 576, 534, 507, 478, 459 cm<sup>-1</sup>.

**Complex 3d:** The following reagents were combined according to the general procedure: *N*-hydroxy-*N,N'*-bis(2-biphenyl)formamidine (0.22 g, 0.62 mmol, 2 equiv.) and Zn<sup>II</sup> acetate·2H<sub>2</sub>O (0.07 g, 0.31 mmol, 1 equiv.). Reaction time: 24 h. The resulting colourless solid was recrystallized from DCM/hexane, yield 0.22 g, 88 %. <sup>1</sup>H NMR (C<sub>6</sub>D<sub>6</sub>, 400 MHz, TMS): δ = 7.40 (d, *J* = 7 Hz, 2 H), 7.38–7.30 (m, 1 H), 7.24 (d, *J* = 7 Hz, 2 H), 7.14–7.09 (m, 6 H), 7.04–6.93 (m, 6 H), 6.88 (t, *J* = 7.0 Hz, 1 H), 6.67 (s, 1 H) ppm. <sup>13</sup>C NMR (C<sub>6</sub>D<sub>6</sub>, 101 MHz, TMS): δ = 149.72, 141.07, 139.12, 136.97, 135.35, 131.33, 130.86, 129.90, 128.98, 128.92, 128.67, 123.80 ppm. C<sub>50</sub>H<sub>38</sub>N<sub>4</sub>O<sub>2</sub>Zn (792.26): calcd. C 75.80, H 4.83, N 7.07; found C 76.30, H 4.95, N 7.14.

**Supporting Information** (see footnote on the first page of this article): <sup>1</sup>H NMR spectra of **2a/3a**, **2b/3b** and **2c/3c**; ORTEP views, spacefill views, H-bonding and intramolecular interactions of **3a**, **3b** and **3d**; cyclic voltammograms of **3b** and **3c**; molecular orbital surfaces for **3a**, **3b** and **3d**; electronic spectra of **3a**, **3b** and **3d**; TD-DFT-calculated singlet transitions for **3a**, **3b** and **3d**; atomic coordinates for DFT optimization of **3a**, **3b** and **3d**.

## Acknowledgments

The authors are grateful to the Natural Sciences and Engineering Research Council (NSERC) of Canada, le Fonds québécois de la recherche sur la nature et les technologies (FRQNT), the Cen-

tre for Self Assembled Chemical Structures (CSACS), and the Université de Montréal for financial support. M. C thanks NSERC for a Canada Graduate Scholarship and FRQNT for a Doctoral Scholarship (A7). The authors also thank Compute Canada and UdeM NMR, EA, XRD, and MS services and personnel for their help.

**Keywords:** Structure elucidation · Zinc · N,O ligands · Substituent effects · Density functional calculations

- [1] C. Kaes, A. Katz, M. W. Hosseini, *Chem. Rev.* **2000**, *100*, 3553–3590.
- [2] U. S. Schubert, A. Winter, G. R. Newkome, *Terpyridine-Based Materials*, Wiley-VCH, Weinheim, Germany, **2011**, p. 65–127.
- [3] H. Furukawa, K. E. Cordova, M. O’Keefe, O. M. Yaghi, *Science* **2013**, *341*.
- [4] a) A. Krajete, G. Steiner, H. Kopacka, K.-H. Ongania, K. Wurst, M. O. Kristen, P. Preishuber-Pfluegl, B. Bildstein, *Eur. J. Inorg. Chem.* **2004**, 1740–1752; b) A. Mishra, M. H. Mohabey, *Asian J. Chem.* **2002**, *14*, 1794–1796; c) A. N. Verma, S. B. Ghose, S. P. Sangal, *J. Indian Chem. Soc.* **1995**, *72*, 685–688; d) L. H. Briggs, R. C. Cambie, I. C. Dean, P. S. Rutledge, *Aust. J. Chem.* **1976**, *29*, 357–366.
- [5] M. Cibian, S. Derossi, G. S. Hanan, *Dalton Trans.* **2011**, *40*, 1038–1040.
- [6] H. A. Goodwin, *Top. Curr. Chem.* **2004**, *234*, 23–47.
- [7] J. Cirera, P. Alemany, S. Alvarez, *Chem. Eur. J.* **2004**, *10*, 190–207.
- [8] H. Xu, R. Chen, Q. Sun, W. Lai, Q. Su, W. Huang, X. Liu, *Chem. Soc. Rev.* **2014**, *43*, 3259–3302.
- [9] a) F. Borbone, U. Caruso, M. Causa, S. Fusco, B. Panunzi, A. Roviello, R. Shikler, A. Tuzi, *Eur. J. Inorg. Chem.* **2014**, 2695–2703; b) U. Caruso, B. Panunzi, A. Roviello, A. Tuzi, *Inorg. Chem. Commun.* **2013**, *29*, 138–140.
- [10] a) G. Yu, S. Yin, Y. Liu, Z. Shuai, D. Zhu, *J. Am. Chem. Soc.* **2003**, *125*, 14816–14824; b) X. Xu, Y. Liao, G. Yu, H. You, C. a. Di, Z. Su, D. Ma, Q. Wang, S. Li, S. Wang, J. Ye, Y. Liu, *Chem. Mater.* **2007**, *19*, 1740–1748; c) R. Wang, L. Deng, M. Fu, J. Cheng, J. Li, *J. Mater. Chem.* **2012**, *22*, 23454–23460.
- [11] a) H.-P. Zeng, G.-R. Wang, G.-C. Zeng, J. Li, *Dyes Pigment.* **2009**, *83*, 155–161; b) L. S. Sapochak, F. E. Benincasa, R. S. Schofield, J. L. Baker, K. K. C. Riccio, D. Fogarty, H. Kohlmann, K. F. Ferris, P. E. Burrows, *J. Am. Chem. Soc.* **2002**, *124*, 6119–6125.
- [12] H.-J. Son, W.-S. Han, J.-Y. Chun, B.-K. Kang, S.-N. Kwon, J. Ko, S. J. Han, C. Lee, S. J. Kim, S. O. Kang, *Inorg. Chem.* **2008**, *47*, 5666–5676.
- [13] a) M. L. Cole, G. B. Deacon, C. M. Forsyth, K. Konstas, P. C. Junk, *Dalton Trans.* **2006**, 3360–3367; b) K. Hirano, S. Urban, C. Wang, F. Glorius, *Org. Lett.* **2009**, *11*, 1019–1022; c) P. Harding, D. J. Harding, H. Adams, S. Youngme, *Synth. Commun.* **2007**, *37*, 2655; d) K. E. Krahulic, G. D. Enright, M. Parvez, R. Roesler, *J. Am. Chem. Soc.* **2005**, *127*, 4142–4143; e) M. Cibian, S. Langis-Barsetti, G. S. Hanan, *Synlett* **2011**, 405–409.
- [14] a) M. Cibian, S. Derossi, G. S. Hanan, *Acta Crystallogr., Sect. E Struct. Rep. Online* **2009**, *65*, o2485; b) E. Baranowska, I. Panfil, C. Belzecki, *Bull. Acad. Pol. Sci., Ser. Sci. Chim.* **1977**, *25*, 93–99; c) C. Belzecki, I. Panfil, *Bull. Acad. Pol. Sci., Ser. Sci. Chim.* **1975**, *23*, 119–123.
- [15] The labelling of the chelate rings is chosen to aid the discussion of the X-ray structures. For some of the atoms, it may differ from the labelling in the corresponding cif file. The structure with full labelling from the cif file is presented in the Supporting Information.
- [16] J. Cirera, E. Ruiz, S. Alvarez, *Inorg. Chem.* **2008**, *47*, 2871–2889.
- [17] F. Allen, *Acta Crystallogr., Sect. B: Struct. Sci.* **2002**, *58*, 380–388.
- [18] CCDC search on August 15, 2015.
- [19] a) Y.-I. Kim, S.-J. Yun, I.-H. Hwang, D.-Y. Kim, S. K. Kang, *Acta Crystallogr., Sect. E Struct. Rep. Online* **2012**, *68*, m504–m505; b) A. I. Poddelsky, I. V. Smolyaninov, A. A. Skatova, A. N. Lukoyanov, G. K. Fukin, N. T. Berberova, V. K. Cherkasov, G. A. Abakumov, *Z. Anorg. Allg. Chem.* **2008**, *634*, 1154–1160; c) A. D. Garnovskii, A. S. Antsyhkina, G. G. Sadikov, I. S. Vasil’chenko, D. A. Garnovskii, A. I. Uraev, M. A. Porai-Koshits, *Zh. Neorg. Khim.* **1995**, *40*, 1977–1980.
- [20] E. P. Ivakhnenko, A. G. Starikov, K. A. Lyssenko, V. I. Ovcharenko, A. S. Bogomyakov, S. L. Veber, V. I. Minkin, *Inorg. Chim. Acta* **2014**, *410*, 144–149.
- [21] D. A. Dickie, R. P. Ulibarri-Sanchez Iii, P. J. Jarman, R. A. Kemp, *Polyhedron* **2013**, *58*, 92–98.
- [22] J. Wolny, Z. Ciunik, M. Rudolf, *J. Chem. Crystallogr.* **1995**, *25*, 407–412.
- [23] a) M. Czugler, R. Neumann, E. Weber, *Inorg. Chim. Acta* **2001**, *313*, 100–108; b) J. Sanmartin-Matalobos, C. Portela-García, L. Martínez-Rodríguez, C. Gonzalez-Bello, E. Lence, A. M. Garcia-Deibe, M. Fondo, *Dalton Trans.* **2012**, *41*, 6998–7004.
- [24] L. Yang, D. R. Powell, R. P. Houser, *Dalton Trans.* **2007**, 955–964.
- [25] C. Di Lulio, M. Middleton, G. Kociok-Köhn, M. D. Jones, A. L. Johnson, *Eur. J. Inorg. Chem.* **2013**, 1541–1554.
- [26] H.-J. Son, W.-S. Han, J.-Y. Chun, B.-K. Kang, S.-N. Kwon, J. Ko, S. J. Han, C. Lee, S. J. Kim, S. O. Kang, *Inorg. Chem.* **2008**, *47*, 5666–5676.
- [27] C.-B. Wu, *Acta Crystallogr., Sect. E: Struct. Rep. Online* **2004**, *60*, m1580–m1581.
- [28] CCDC search on September 8, 2015.
- [29] N. G. Connelly, W. E. Geiger, *Chem. Rev.* **1996**, *96*, 877–910.
- [30] M. Cibian, S. Langis-Barsetti, F. G. De Mendonça, S. Touaibia, S. Derossi, D. Spasyuk, G. S. Hanan, *Eur. J. Inorg. Chem.* **2015**, 73–82.
- [31] J. A. Wolny, M. F. Rudolf, Z. Ciunik, K. Gatner, S. Wolowiec, *J. Chem. Soc., Dalton Trans.* **1993**, 1611–1622.
- [32] a) J.-L. Bredas, *Mater. Horiz.* **2014**, *1*, 17–19; b) P. I. Djurovich, E. I. Mayo, S. R. Forrest, M. E. Thompson, *Org. Electron.* **2009**, *10*, 515–520.
- [33] C. Adamo, D. Jacquemin, *Chem. Soc. Rev.* **2013**, *42*, 845–856.
- [34] M. J. Frisch, G. W. Trucks, H. B. Schlegel, G. E. Scuseria, M. A. Robb, J. R. Cheeseman, G. Scalmani, V. Barone, B. Mennucci, G. A. Petersson, H. Nakatsuji, M. Caricato, X. Li, H. P. Hratchian, A. F. Izmaylov, J. Bloino, G. Zheng, J. L. Sonnenberg, M. Hada, M. Ehara, K. Toyota, R. Fukuda, J. Hasegawa, M. Ishida, T. Nakajima, Y. Honda, O. Kitao, H. Nakai, T. Vreven, J. A. Montgomery Jr., J. E. Peralta, F. Ogliaro, M. Bearpark, J. J. Heyd, E. Brothers, K. N. Kudin, V. N. Staroverov, R. Kobayashi, J. Normand, K. Raghavachari, A. Rendell, J. C. Burant, S. S. Iyengar, J. Tomasi, M. Cossi, N. Rega, J. M. Millam, M. Klene, J. E. Knox, J. B. Cross, V. Bakken, C. Adamo, J. Jaramillo, R. Gomperts, R. E. Stratmann, O. Yazyev, A. J. Austin, R. Cammi, C. Pomelli, J. W. Ochterski, R. L. Martin, K. Morokuma, V. G. Zakrzewski, G. A. Voth, P. Salvador, J. J. Dannenberg, S. Dapprich, A. D. Daniels, Ö. Farkas, J. B. Foresman, J. V. Ortiz, J. Cioslowski, D. J. Fox, *Gaussian 09*, revision D.01, Gaussian, Inc., Wallingford CT, **2009**.
- [35] a) C. Lee, W. Yang, R. G. Parr, *Phys. Rev. B* **1988**, *37*, 785–789; b) B. Miehlich, A. Savin, H. Stoll, H. Preuss, *Chem. Phys. Lett.* **1989**, *157*, 200–206.
- [36] M. M. Francl, W. J. Pietro, W. J. Hehre, J. S. Binkley, M. S. Gordon, D. J. DeFrees, J. A. Pople, *J. Chem. Phys.* **1982**, *77*, 3654–3665.
- [37] J. Tomasi, B. Mennucci, R. Cammi, *Chem. Rev.* **2005**, *105*, 2999–3094.
- [38] a) M. E. Casida, C. Jamorski, K. C. Casida, D. R. Salahub, *J. Chem. Phys.* **1998**, *108*, 4439–4449; b) R. E. Stratmann, G. E. Scuseria, M. J. Frisch, *J. Chem. Phys.* **1998**, *109*, 8218–8224.
- [39] R. D. K. Dennington II, T. Keith, J. Millam, K. Eppinnett, W. L. Hovell, R. Gilliland, *GaussView*, v. 3.0.9, Semichem, Inc., Shawnee Mission, KS, **2003**.
- [40] N. M. T. O’Boyle, A. L. K. M. Langner, *J. Comput. Chem.* **2008**, *29*, 839–845.
- [41] L. Skripnikov, *Chemission*, v. 4.36, **2005–2015**.

Received: September 29, 2015

Published Online: December 11, 2015